Chemical Engineering Journal 532 (2026) 174335

Contents lists available at ScienceDirect

Chemical Engineering Journal

journal homepage: www.elsevier.com/locate/cej

Synergistic thermoelectric enhancement enabled by metalated porphyrin-pyrene porous organic polymer/carbon nanotube composites

Tzu-Ling Ma [a,1], Mohamed Gamal Mohamed [b,1], Hira Karim [c], Shiao-Wei Kuo [b,*], Cheng-Liang Liu [a,d,**]

[a] Department of Materials Science and Engineering, National Taiwan University, Taipei 10617, Taiwan
[b] Department of Materials and Optoelectronic Science, Center for Functional Polymers and Supramolecular Materials, National Sun Yat-Sen University, Kaohsiung 80424, Taiwan
[c] Department of Chemistry, School of Natural Sciences (SNS), National University of Sciences and Technology (NUST), H-12, Islamabad 44000, Pakistan
[d] Advanced Research Center for Green Materials Science and Technology, National Taiwan University, Taipei 10617, Taiwan

ARTICLE INFO

Keywords:
Thermoelectric
Porous organic polymers
Porphyrin
Carbon nanotubes
Composite
Metal coordination

ABSTRACT

Porous organic polymers (POPs), characterized by intrinsic porosity, structural tunability, and low thermal conductivity, offer promising potential for thermoelectric (TE) applications. Herein, a porphyrin-pyrene-based POP (Por-Py POP) is designed to integrate the extended π-conjugation and metal-coordination capability of porphyrins with the planar π-rich architecture of pyrene, thereby promoting charge transport. Post-synthetic metalation with Fe^{2+}, Cu^{2+}, or Zn^{2+} further introduces d_{π}-π orbital interactions, thereby strengthening the interfacial coupling with single-walled carbon nanotubes (CNTs) and facilitating efficient charge transfer. Among the resulting composites, the ZnPor-Py POP/CNT exhibits a power factor (*PF*) of 55.8 ± 6.3 μW m^{-1} K^{-2}, which represents a 40% improvement over the non-metalated analogue and is attributed to an enhanced electrical conductivity (σ) via d_{π}-π orbital interactions. Meanwhile, the porous POP framework contributes to suppressing lattice thermal transport relative to pristine CNTs, resulting in a thermal conductivity (κ) of 8.8 ± 0.2 W m^{-1} K^{-1} for the ZnPor-Py POP/CNT composite and an improved figure of merit (zT) of 1.89 × 10^{-3} ± 0.22 × 10^{-3} at 300 K, corresponding to a 8.6% enhancement over pristine CNTs. Overall, this work demonstrates a synergetic design strategy that combines metal coordination for σ enhancement and porous frameworks for κ suppression, thus providing a versatile pathway toward next-generation high-performance porous composite TE materials.

1. Introduction

In the era of rapid artificial intelligence (AI) development, global electricity demand is experiencing unprecedented growth. According to the International Energy Agency (IEA), this surge is primarily driven by expanding industrial activity, the electrification of transportation, the rapid growth of data centers, and AI-driven computing [1]. However, as nearly 67% of electricity is still being generated from fossil fuels with limited conversion efficiency, a large proportion of primary energy is inevitably lost as waste heat [2]. In particular, low-grade thermal energy (with temperatures below 100 °C) accounts for more than 30% of global primary energy consumption but remains underutilized, corresponding to an estimated 85 petawatt-hours (PWh) of wasted energy annually [3]. To address this problem, various energy conversion technologies have emerged, with thermoelectric (TE) systems offering a particularly compelling solution by directly converting waste heat into electricity without the need for moving parts and without greenhouse gas emissions. Moreover, continuous advances in material design are expanding the potential of TE systems for sustainable energy harvesting [4]. In the pursuit of high efficiency TE materials, their performance is typically evaluated by using the figure of merit (zT), which is defined by Eq. (1):

$$zT = S^2\sigma T \kappa^{-1} \quad (1)$$

where S is the Seebeck coefficient, σ is the electrical conductivity, T is the absolute temperature, and κ is the thermal conductivity. The term $S^2\sigma$ is commonly referred to as the power factor (*PF*). Achieving a high

* Corresponding author.
** Correspondence to: C.-L. Liu, Department of Materials Science and Engineering, National Taiwan University, Taipei, 10617, Taiwan.
E-mail addresses: kuosw@faculty.nsysu.edu.tw (S.-W. Kuo), liucl@ntu.edu.tw (C.-L. Liu).
[1] These authors contributed equally to this work.

https://doi.org/10.1016/j.cej.2026.174335
Received 21 November 2025; Received in revised form 21 January 2026; Accepted 17 February 2026
Available online 18 February 2026

zT, therefore, requires simultaneous optimization of these interdependent parameters, which is a challenging task due to the inherent trade-offs [5]. For instance, enhancing the electrical conductivity often leads to a higher thermal conductivity and diminished Seebeck coefficient [6]. Consequently, composites that decouple charge and phonon transport have emerged as a promising design strategy for high-performance TE materials [5–7]. Inorganic alloy TE materials such as Bi_2Te_3, PbTe, and SiGe [8] have demonstrated high zT at mid-to-high temperatures, but their limited performance near room temperature ($zT < 1$), combined with drawbacks such as toxicity, high cost, rigidity, and poor processability, restricts their practical application in flexible TE devices [9]. To address these challenges, carbon-based nanomaterials (particularly single-walled carbon nanotubes, CNTs) have gained attention due to their high electrical conductivity, mechanical flexibility, and one-dimensional charge transport characteristics [10–11]. However, their intrinsically low Seebeck coefficient (<30 μV K^{-1}) and high thermal conductivity still limit their TE performance [9,12]. Moreover, their processability and scalability are impeded by poor CNT dispersion in solution. Hence, various conducting polymers have been incorporated to form polymer/CNT composites via solution processing to enhance the CNT dispersion, interfacial interactions, and TE performance [13]. For instance, composites such as poly(3,4-ethylenedioxythiophene): poly (styrene sulfonate) (PEDOT: PSS)/CNTs (PF = 300 μW m^{-1} K^{-2}) [14], poly(3-hexylthiophene) (P3HT)/CNTs (PF = 49 μW m^{-1} K^{-2}) [15], and polyaniline (PANI)/CNTs (PF = 401 μW m^{-1} K^{-2}) [16] have been reported. In addition, the present research group has developed several polythiophene-derivative/CNT composite systems with comparable or improved performance [17–19].

Despite these advances, the thermal conductivity of such polymer/CNT composites is often overlooked, thereby limiting their true zT potential. To mitigate this issue, recent strategies have incorporated porous structures into CNT-based systems in order to enhance phonon scattering and introduce structural disorder, thereby reducing the thermal conductivity [20–22]. In particular, crystalline metal-organic frameworks (MOFs) have been widely studied due to their tunable nanoporous architectures, coordinated transition metal centers, and organic ligands, which make them promising platforms for thermal conductivity suppression [23–24]. For example, Chen et al. demonstrated the in-situ growth of ZIF-67/carboxylated CNT composites with a thermal conductivity of 4.1 W m^{-1} K^{-1} and a zT of 0.02 [25]. Similarly, the present research group previously developed ZrBTB-BA10/CNT composites with a thermal conductivity of 4.3 W m^{-1} K^{-1} and an optimal zT of 0.029 [26]. More recently, porous organic polymers (POPs), including crystalline covalent organic frameworks (COFs) and amorphous conjugate microporous polymers (CMPs) [27–28], have emerged as attractive alternatives due to their low weight, high structural tunability, and enhanced chemical/thermal stability. The amorphous nature of POPs further promotes phonon scattering, which can potentially suppress lattice thermal conductivity more effectively than their crystalline analogues [28–30]. Nevertheless, despite their extensive use in supercapacitors [31], photovoltaics [32], electrocatalysts [33], and sensors [34], their inherently low electrical conductivity remains a limitation for TE applications.

Although POPs can be synthesized from diverse building blocks, thereby enabling control over their electronic structure and functionality, precise structural tailoring remains a critical challenge for performance optimization [29]. Among various molecular motifs, porphyrins are especially appealing due to their 18 π-electron aromatic macrocycles, four pyrrolic nitrogen-donor sites, and versatile metal coordination capability. These features allow for tunable redox properties and stable electronic structures in porous frameworks with extended conjugation [35–37]. Simulations have further revealed that coordinated metal ions modulate conductance in porphyrin molecular wires and that Zn-porphyrin nanotubes with asymmetric bandgaps can boost the thermopower and electronic performance [38–39]. Meanwhile, the polycyclic aromatic hydrocarbon pyrene features a planar, π-rich architecture that is conducive to strong π-π stacking and effective charge transport [40–42]. Moreover, study has shown that metalloporphyrin monomers can strengthen the d_π-π orbital interactions with CNTs in order to facilitate charge transfer and enhance the electrical conductivity [43]. Consequently, the incorporation of metalloporphyrin and pyrene into a single π-conjugated POP provides a collaborative platform for improving the interfacial interactions and charge transport in CNT-based TE materials for enhanced electrical conductivity.

To integrate the above concepts, the present study reports the design and synthesis of a porphyrin-pyrene-based POP (Por-Py POP) via Schiff-base condensation, followed by post-synthetic metalation with Fe^{2+}, Cu^{2+}, or Zn^{2+}. The resulting metalated Por-Py POPs (designated MPor-Py POPs) are then hybridized with CNTs to enhance the electrical conductivity via π-π and d_π-π orbital interactions. The amorphous and intrinsically porous structure further promotes phonon scattering and reduces the thermal conductivity. Density functional theory (DFT) calculations are conducted to assess the metal binding energies within the porphyrin core and evaluate potential interactions with the CNTs. Among the as-prepared composites, the ZnPor-Py POP/CNT achieves the highest PF of 55.8 μW m^{-1} K^{-2}, which is attributed to the enhanced electrical conductivity via efficient metal-CNT d_π-π orbital interactions. In addition, its porous framework contributes to a reduced thermal conductivity of 8.84 W m^{-1} K^{-1}, thereby resulting in an improved zT of 1.89×10^{-3} at 300 K, representing a 9.8% enhancement over the pristine CNTs. Furthermore, this composite is successfully integrated into a flexible TE generator (TEG), demonstrating both excellent mechanical stability and reliable thermal-to-electric energy conversion. Overall, this work highlights a synergistic approach that combines metal coordination for enhanced electrical conductivity with a porous framework for the suppression of thermal conductivity, thereby advancing the design of next-generation porous composite TE materials.

2. Experimental section

2.1. Materials

Anhydrous ethanol (EtOH, 99.8%), 5,10,15,20-tetrakis(4-bromophenyl)porphyrin (porphyrin-4Br), and zinc acetate ($Zn(OAc)_2$, 99%) were purchased from Acros Organic. 1,2-dichlorobenzene (DCB, anhydrous 99%) and *N*-methyl-2-pyrrolidone (NMP, anhydrous, 99.5%) were acquired from Sigma-Aldrich. Copper(II) acetate anhydrous ($Cu(OAc)_2$, 98%) and iron(II) chloride anhydrous ($FeCl_2$, 99.5%) were obtained from Alfa Aesar. Single-walled carbon nanotubes (CNTs, purity >95%, diameter 1-2 nm, length 5–30 μm) were supplied by XFNANO. All chemicals were used as received without further purification. 1,3,6,8-tetrabromopyrene (Py-4Br), and 1,3,6,8-tetrakis((4-aminophenyl)ethynyl)pyrene (Py-$4NH_2$) were carried out according to previously reported procedures, with slight modifications [41,44,45].

2.2. Syntheses of 4′,4‴,4⁗,4⁗′-(porphyrin-5,10,15,20-tetrayl)tetrakis (([1,1′-biphenyl]-4-carbaldehyde)) (Por-4CHO)

Porphyrin-4Br (0.67 g, 0.73 mmol), the appropriate co-reactant 4-formylphenylboronic acid (0.87 g, 5.10 mmol), $Pd(PPh_3)_4$ (45 mg, 0.04 mmol), and K_2CO_3 (1.00 g, 7.28 mmol) were introduced into a 100 mL round-bottom flask. The flask was degassed under vacuum for 20 min and subsequently purged with nitrogen. Anhydrous DMF (40 mL) was added under an inert atmosphere, and the reaction mixture was stirred at 110 °C for 72 h under nitrogen. Upon completion of the reaction, as confirmed by TLC, the mixture was cooled to ambient temperature and poured into ice-cold water (400 mL). The formation of a violet solid was observed immediately. The precipitate was isolated by filtration and thoroughly washed with water, methanol, and dichloromethane to remove K_2CO_3 and residual organic impurities. The final product was dried under reduced pressure to yield Por-4CHO as a violet powder.

2.3. Synthesis of Por-Py POP

As shown in Scheme 1(a), to prepare Por-Py POP, PT-4NH_2 (0.06 g, 0.09 mmol) and Por-4CHO (0.09 g, 0.09 mmol) were combined in a 10 mL Schlenk tube, with n-butanol (4.5 mL), 1,2-dichlorobenzene (DCB, 4.5 mL), and acetic acid (0.9 mL, 6 M). After degassing by three freeze–pump–thaw cycles under vacuum, the sealed vessel was heated at 115 °C for 180 h. The resulting solid was isolated by filtration and purified by Soxhlet extraction with DMF and acetone. The final product, a dark reddish-brown powder, was identified as Por-Py POP. Solid-state ^{13}C NMR analysis: 151.4 ppm (C=N), 111.4–147.1 ppm (aromatic carbon atoms), 88.0 and 98.3 ppm (C≡C).

2.4. Metalation of Por-Py POP (MPor-Py POP)

As shown in Scheme 1(b), Por-Py POP (40 mg) and EtOH (4 mL) were placed in a 50 mL round-bottom flask and dispersed by ultrasonication for 5 min. The mixture was then stirred at 400 rpm at room temperature. Subsequently, the metal salt solution, 40 mg of $FeCl_2$ (or $Cu(OAc)_2$ or $Zn(OAc)_2$) dissolved in 4 mL of EtOH, was added dropwise into the flask. The final reaction mixture was heated to 60 °C and maintained for 24 h. After the metalation, the mixture was cooled to room temperature, followed by purification through vacuum filtration and rinsing with EtOH. The final product was dried in a vacuum oven at 85 °C overnight to ensure the residual solvent was removed. Yield: FePor-Py POP (60 mg), CuPor-Py POP (58 mg), ZnPor-Py POP (28 mg).

2.5. Preparation of composite thin film

The composite thin films fabrication process is illustrated in Scheme S1. All Por-Py POPs or MPor-Py POPs and CNTs were pre-dried in a vacuum oven at 100 °C overnight to remove residual moisture. Subsequently, 1.5 mg of Por-Py POP (or MPor-Py POP) was dispersed in 1.5 mL of anhydrous DCB via ultrasonication for 1 h. The dispersion was then transferred into a ball mill jar containing grinding balls, 1.5 mg of CNTs, and an additional 1.5 mL of DCB. The mixture was homogenized using a Retsch MM440 ball mill operating at 30 Hz for 15 min. This yielded 3 mL of a homogeneous composite dispersion with a 1/1 weight ratio of MPor-Py POP to CNTs. Similarly, dispersions with weight ratios of 1/2 and 2/1 (MPor-Py POP/CNT) were also prepared following the same protocol. Each composite solution (70 μL) was drop-casted twice onto the 7 × 15 mm^2 O_3-plasma-treated glass substrate. The films were dried at 120 °C in a nitrogen-filled glovebox and subsequently annealed at 190 °C for 15 min under a nitrogen atmosphere to ensure complete

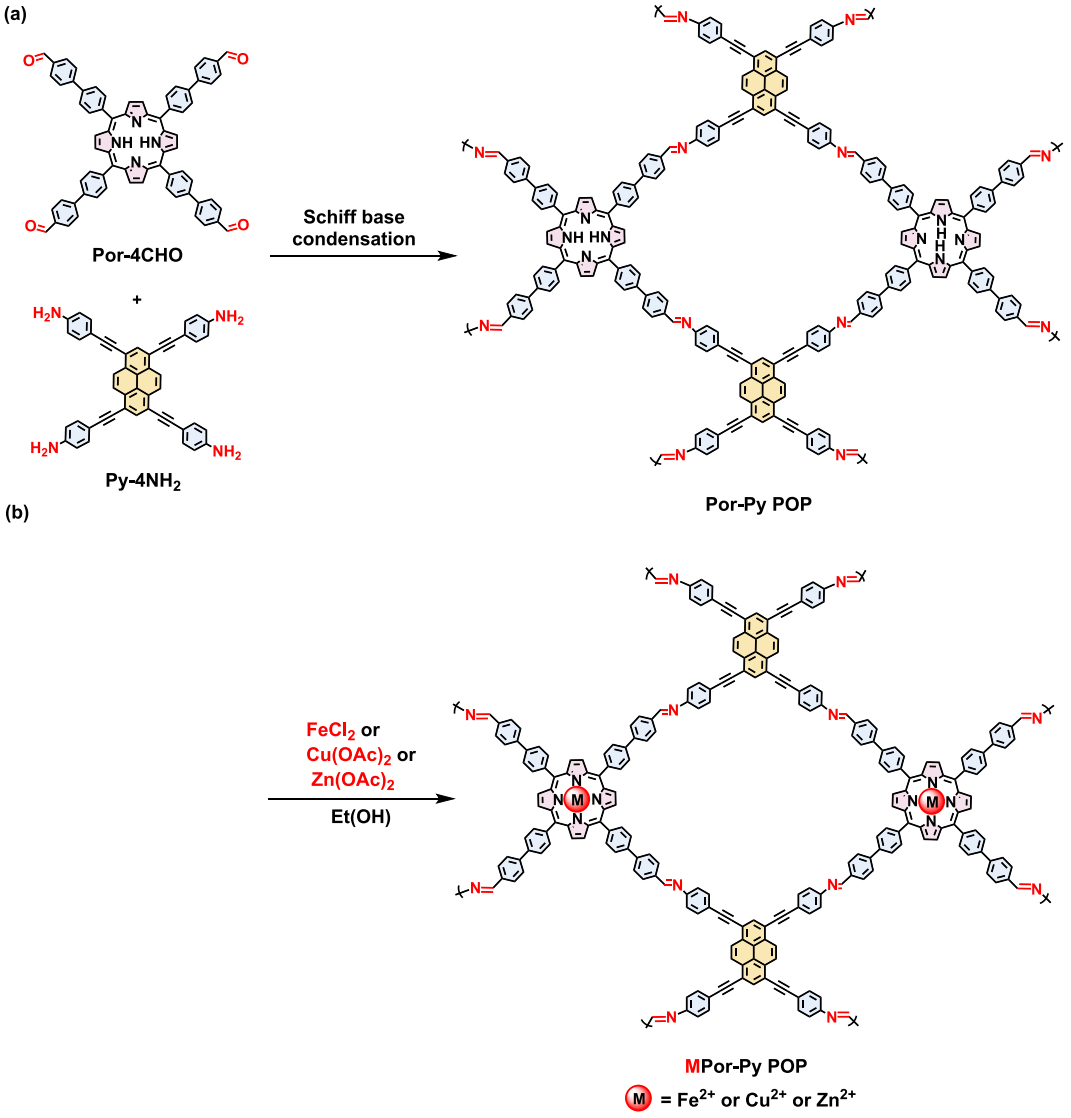

Scheme 1. (a) Synthetic route of Por-Py POP via the Schiff-base condensation. (b) Post-synthetic metalation of the Por-Py POP using divalent metal salts (Fe^{2+}, Cu^{2+}, or Zn^{2+}) to yield MPor-Py POPs with coordinated metal centers embedded within the porphyrin macrocycles.

removal of residual solvent. The resulting composite films exhibited uniform thicknesses of approximately 5–6 μm.

2.6. Fabrication of the thermoelectric generator

To fabricate the TEG device, the ZnPor-Py POP/CNT composite solution was drop-casted twice (140 μL per cast) onto eight polyimide strips (7 × 30 mm^2), each pre-treated with O_3 plasma. The films were dried at 120 °C inside a nitrogen glovebox and subsequently adhered to a flexible polyethylene terephthalate (PET) substrate (10 × 5 cm^2) with a 5 mm spacing between adjacent strips. Silver paste was applied to both ends of each strip to form electrical contacts, and copper wires were used to interconnect the strips for integration into an external circuit.

2.7. Characterization of thermoelectric properties

A ZEM-3 thermoelectric measurement system (Advance Riko) was employed to determine the in-plane Seebeck coefficient (S) and electrical conductivity (σ) of drop-cast non-metalated and metalated Por-Py POP/CNT composite films at 303 K within a helium-filled chamber. Film thicknesses were determined using a KLA Alpha-Step® D-300 surface profilometer. Thermal diffusivity (α) was measured in the in-plane direction using a TA-3 thermowave analyzer (Bethel Co., Ltd., Japan) on freestanding films (1.2 × 1.2 mm^2). Specific heat capacity (Cp) of the composites was determined via a differential scanning calorimetry (DSC25, TA Instruments) at a scan rate of 10 °C min^{-1}, utilizing sapphire for calibration. Subsequently, the thermal conductivity (κ) was derived from the formula $\kappa = \rho \cdot \alpha \cdot Cp$, where ρ denotes the density of the composite films. All thermoelectric parameters, including Seebeck coefficient (S), electrical conductivity (σ), and thermal conductivity (κ), were measured using at least three independent specimens ($n = 3$) for each composition. The performance of the thermoelectric generators (TEGs) was evaluated by recording the output voltage through a Keithley 2182A nanovoltmeter (Tektronix, USA) equipped with probe tips. To establish controlled temperature gradients, Peltier plates were utilized, with their respective temperatures monitored via thermocouples integrated into the probes. Data collection, including the calculation of temperature differentials, was handled by a Keithley DAQ6510 multimeter system. Furthermore, a FLIR A50 thermal infrared camera (Teledyne FLIR LLC, USA) was employed to track the temperature gap between human skin and the ambient environment for practical application assessments.

3. Results and discussion

3.1. Synthesis and characterization of porous organic polymer (Por-Py POP)

The synthetic route for the novel imine-linked Por-Py POP is depicted in Scheme 1(a) and described in detail in the Experimental section (Synthesis of Por-Py POP). The starting monomer, Por-4CHO, was characterized by Fourier-transform infrared (FTIR) spectroscopy and ^1H and ^{13}C nuclear magnetic resonance (NMR) spectroscopy, as shown in Figs. S1 and S2. As presented in Fig. S1, Por-4CHO exhibits characteristic vibrational bands at 3028 cm^{-1}, corresponding to sp^2 C—H stretching, and at 2725–2812 cm^{-1}, which are attributed to the C—H stretching vibrations of the aldehyde group. In addition, distinct absorption bands at 1600 cm^{-1} and 1702 cm^{-1} are assigned to C═C stretching of the conjugated porphyrin framework and the C═O stretching of the aldehyde functionality, respectively. The ^1H NMR spectrum of Por-4CHO [Fig. S2(a)] exhibits a characteristic resonance at 10.16 ppm assigned to the aldehyde proton (H-C═O), while the signals at 8.94 ppm are attributed to the β-pyrrolic protons of the porphyrin ring. In addition, a set of resonances in the range of 7.77–8.34 ppm corresponds to the aromatic protons. Furthermore, the ^{13}C NMR spectrum [Fig. S2(b)] reveals resonances in the range of 125.6–135.9 ppm associated with aromatic carbons, as well as a distinct signal at 191.9 ppm corresponding to the aldehyde carbon. These spectroscopic features collectively confirm the successful synthesis of Por-4CHO and demonstrate its suitability as a highly conjugated building block for constructing POP via Schiff-base condensation. In brief, Py-4NH_2 and Por-4CHO undergo a catalyst-free [4 + 4] Schiff-base condensation to afford the targeted Por-Py POP. The reaction was conducted in a mixed solvent system of n-butanol and 1,2-dichlorobenzene (DCB), with 6 M acetic acid serving as a promoter, thereby resulting in the successful formation of the imine-linked Por-Py POP framework. The successful Schiff-base condensation is confirmed by the solid-state ^{13}C nuclear magnetic resonance (NMR) spectrum of the Por-Py POP in Fig. S3, which displays distinct resonances at 111.4–147.1, 151.4 and 190.7 ppm, corresponding to extended aromatic carbons C═N units and terminal group derived from Por-4CHO monomer, respectively, along with characteristic signals at 88.0 and 98.3 ppm due to the C≡C bonds of the pyrene moiety [41].

To evaluate the porosity of the Por-Py POP, the N_2 adsorption/desorption isotherms were measured at 77 K, and the results are shown in Fig. 1(a). At a low relative pressure ($P/P_0 < 0.1$), the isotherm exhibits a sharp uptake with a convex upward profile attributed to micropore filling, thereby indicating strong van der Waals interactions between N_2 molecules and the porous framework [46,47]. The isotherm displays a typical type IV profile with capillary condensation behavior, which is characteristic of mesoporous materials as defined by the International Union of Pure and Applied Chemistry (IUPAC) [47]. Further, a H3 or H4 type hysteresis loop is observed, thereby suggesting the presence of slit-shaped mesopores with a broad pore size distribution [48,49]. These observations confirm the hierarchical porous nature of the Por-Py POP. The specific surface area (SA_{BET}) is calculated to be 182 m^2 g^{-1}, with a total pore volume (V_{total}) of 0.21 cm^3 g^{-1}. The pore size distribution, derived via the non-local density functional theory (NLDFT) model [50], is shown in Fig. 1(b). This reveals a bimodal distribution with ranges of 0.80–1.96 nm and 2.04–3.42 nm, thereby indicating the coexistence of both micropores and mesopores, respectively, within the polymer matrix. The scanning electron microscopy (SEM) image in Fig. 1(c) reveals a particulate morphology composed of interconnected, irregularly shaped nanoscale spheres, forming a rough but continuous network that may enhance the interfacial interactions in composite formulations. Further, the energy-dispersive X-ray spectroscopy (EDS) elemental mappings in Fig. 1(d)–(f) confirm the homogeneous spatial distributions of carbon (C; white), nitrogen (N; red), and oxygen (O; blue) atoms throughout the Por-Py POP polymeric framework, which is consistent with the proposed chemical structure and successful incorporation of the porphyrin and pyrene units. Moreover, the XPS analysis yields elemental concentrations of C (95.11%), N (1.40%), and O (3.49%) in Fig. S4 and Table S1. The alignment between XPS and EDS results validates the elemental distribution and compensates for the technical constraints of SEM-EDS mapping.

3.2. Synthesis and characterization of metalated porous organic polymers

As illustrated in Scheme 1(b), the metalation of the porphyrin core is achieved via coordination of Fe^{2+}, Cu^{2+}, or Zn^{2+} ions with the electron-donating nitrogen atoms, where $FeCl_2$, $Cu(OAc)_2$, or $Zn(OAc)_2$ respectively react with Por-Py POP in the presence of ethanol (EtOH) to form stable metalloporphyrin units, in accordance with previous reports [51-54]. The successful metalation of the Por-Py POP is confirmed by the Fourier-transform infrared (FTIR) spectroscopy, thermogravimetric analysis (TGA), ultraviolet-visible-near-infrared (UV–vis-NIR) spectroscopy, inductively coupled plasma-mass spectrometry (ICP-MS), and X-ray photoelectron spectroscopy (XPS) results in Fig. 2. Thus, in Fig. 2(a), the FTIR spectrum of the non-metalated Por-Py POP exhibits prominent vibrational features at 3300 cm^{-1} and 1465–1513 cm^{-1}, corresponding to the N—H stretching and pyrrole ring vibrations of the porphyrin moiety [35]. In addition, a distinct C≡C band at 2194 cm^{-1} is attributed to the pyrene unit, while the presence of a sharp C═N stretching band at 1619 cm^{-1} confirms successful imino group formation via Schiff base

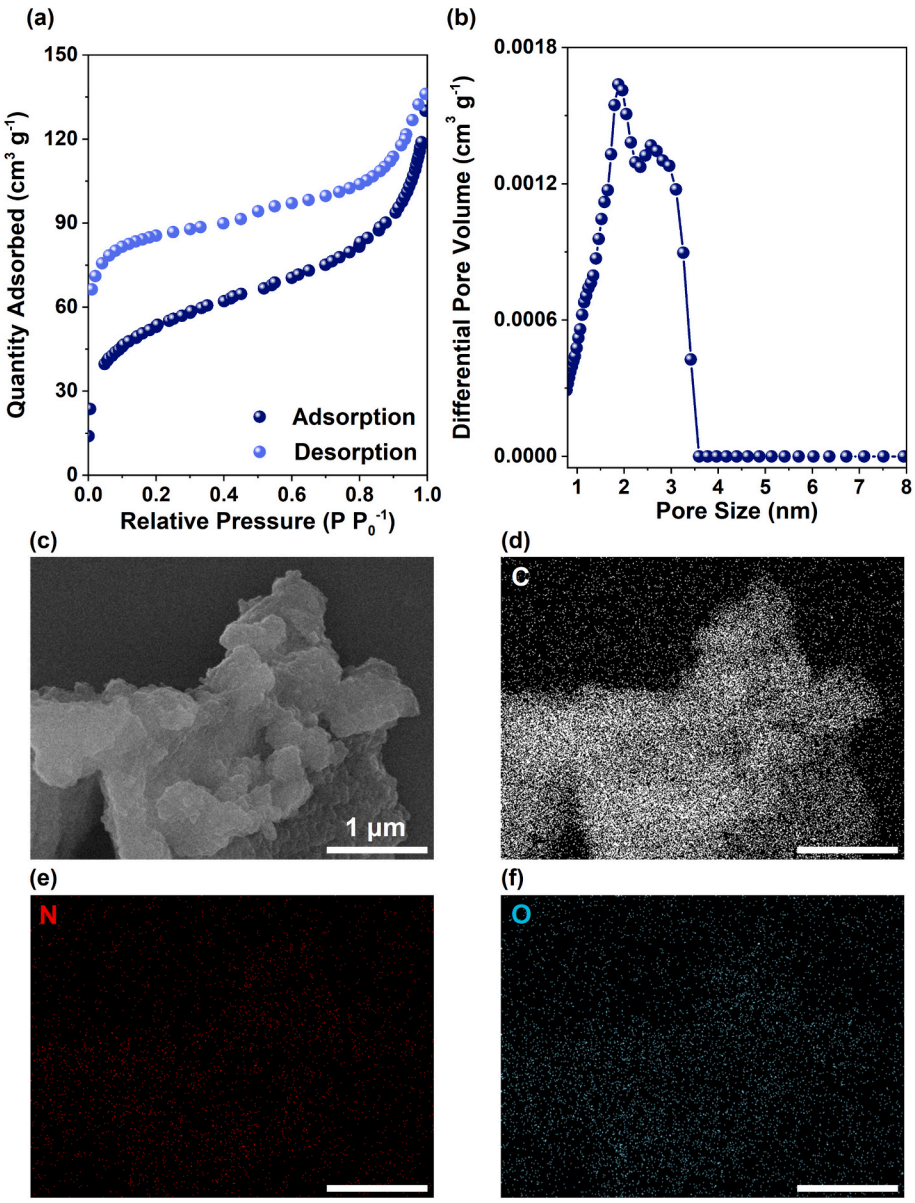

Fig. 1. (a) N_2 adsorption/desorption isotherm, (b) pore size distribution, and (c) SEM image of Por-Py POP. SEM-EDS elemental mapping images of Por-Py POP showing the distribution of: (d) C, (e) N, and (f) O. All scale bars correspond to 1 μm.

condensation. Further, the intense peak at 1600 cm^{-1} corresponds to the aromatic C═C stretching vibration, indicating the extended π-conjugated framework. Upon metalation, these characteristic peaks remain unchanged, indicating that the POP backbone is well preserved. Notably, the N—H vibration of the inner pyrrole ring disappears, while a pronounced metal-nitrogen (M–N) vibrational feature appears near 1000 cm^{-1} (highlighted in Fig. S5), thereby confirming the coordination of metal ions with the porphyrin core [55,56]. The excellent thermal stability of the Por-Py POP is demonstrated by the TGA results in Fig. 2 (b), where the 5% and 10% weight loss temperatures (T_{d5} and T_{d10}) are 433 and 508 °C, respectively, and the char yield reaches 58.9 wt% at 700 °C. Following metalation, the residual mass increases to 72.6, 69.6, and 62.1 wt% for the FePor-Py POP, CuPor-Py POP, and ZnPor-Py POP, indicating enhanced thermal robustness due to metal incorporation into the porphyrin framework [53,54]. A similar trend is also observed in TGA measurements conducted under air, as shown in Fig. S6. The degree of metalation was quantified by ICP-MS analysis (Tables S2–S4). Among the three metal ions, Fe^{2+} displays the highest coordination efficiency, with 77.2% metalation of the porphyrin units, followed by Cu^{2+} (52.3%) and Zn^{2+} (29.9%). This trend is visually corroborated by the degree of fluorescence quenching observed under 365 nm UV irradiation in Fig. S7, where the FePor-Py POP exhibits the most pronounced quenching behavior, attributed to efficient photoinduced electron or energy transfer between the Fe ions and porphyrin π-system. All metalated variants display varying degrees of fluorescence quenching (Fig. S8), reflecting differences in coordination strength and charge redistribution, which are expected to influence thermoelectric performance upon CNT hybridization, as discussed in Section 3.4. The UV–vis absorption spectra of the POPs are presented in Fig. 2(c). All samples exhibit the characteristic porphyrin features, including a distinctive B (Soret) band at around 425 nm and four weak Q bands at 509, 555, 598, and 655 nm associated with π-π* transitions of the electrons in the porphyrin structure from the ground state to the second excited state ($S_0 \rightarrow S_2$) and from the ground state to the first excited state ($S_0 \rightarrow S_1$) [57,58]. Additionally, absorption peaks are observed at 378 and 358 nm due to the pyrene moiety, which contributes to the extended π-conjugation within the framework [59]. Upon metalation, however, the four Q bands decrease in intensity relative to the non-metalated Por-Py POP,

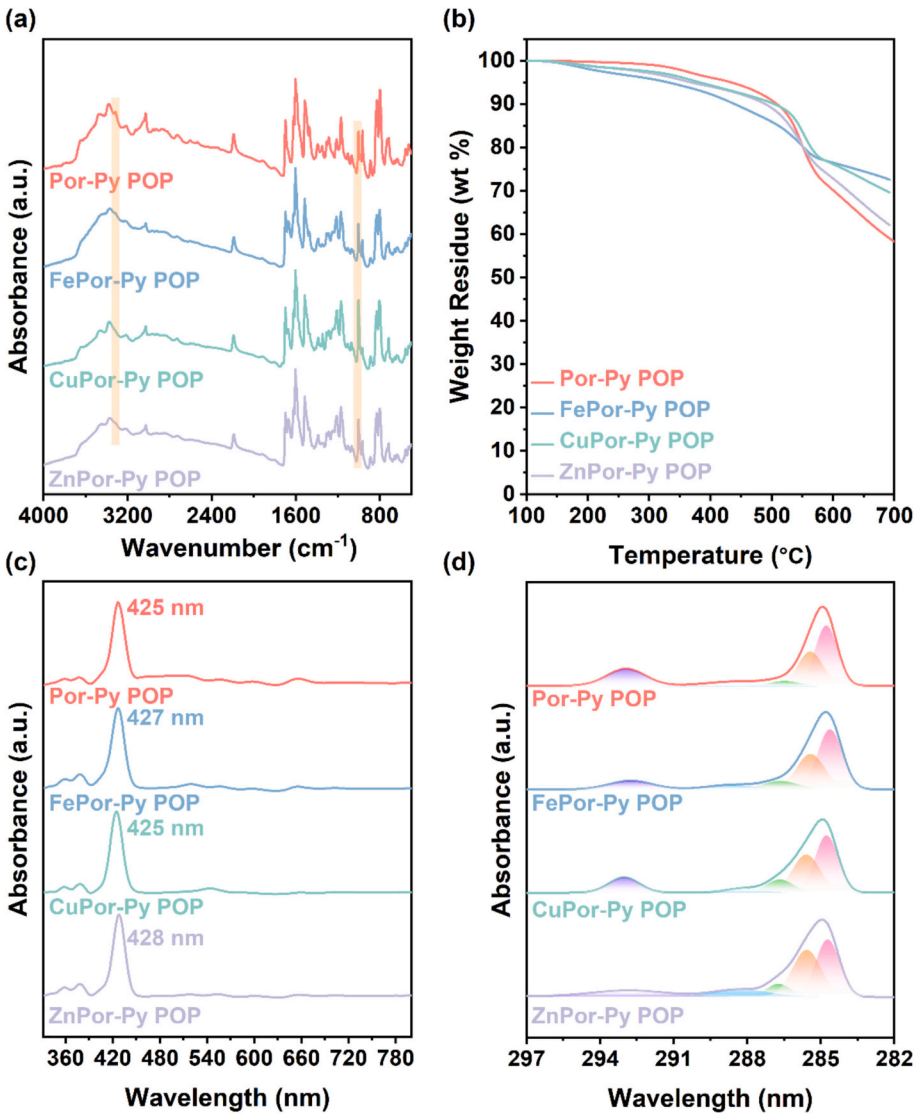

Fig. 2. (a) FTIR spectra, (b) TGA profiles under N_2 condition, (c) UV–Vis absorption spectra, and (d) XPS C1s deconvolution profiles of Por-Py POP (red line), FePor-Py POP (blue line), CuPor-Py POP (green line), and ZnPor-Py POP (purple line).

consistent with successful incorporation of metal ions into the porphyrin structure [60]. Notably, the ZnPor-Py POP exhibits a more pronounced red shift of the B band, indicative of enhanced π-delocalization and electron density redistribution induced by Zn^{2+} coordination within the porphyrin ring [60,61]. These spectral changes are not only consistent with successful metalation but also have significant implications for TE applications. The enhanced π-delocalization and modified electronic structures can facilitate more efficient charge transfer by improving both the charge carrier mobility and density. In particular, the observed red shift and band broadening in the ZnPor-Py POP indicate enhanced π-conjugation within the porphyrin ring, which facilitates more efficient charge transport upon hybridization with CNTs, as discussed in Section 3.4 below.

XPS analysis further confirms metal incorporation and coordination displays in Figs. 2(d), S9, and Table S1. Thus, the full survey spectra of the various MPor-Py POPs exhibit peaks due to C 1s, N 1s, and O 1s, along with the selected metal species (Fe 2p, Cu 2p, and Zn 2p) (Table S1). Further, the high-resolution C 1s spectra in Fig. 2(d) display five deconvoluted peaks at 284.8, 285.4, 286.5, 288.3, and 292.9 eV, corresponding to C–C/C=C, C≡C, C—N, C═N, and the π-π* shake-up satellite, respectively, which are characteristic of aromatic and conjugated systems [62,63]. Meanwhile, the N1s spectra in Fig. S9(a) reveal two main peaks at 398.7 and 400.4 eV, which are attributed to the respective –NH– and = N– groups [60]. Notably, upon metalation, the intensity of the –NH– peak decreases, particularly for the FePor-Py POP, confirming metal coordination. Further validation of metal oxidation states is provided by the high-resolution Fe 2p, Cu 2p, and Zn 2p spectra in Fig. S9(b)–(d) [64,65]. Importantly, the absence of satellite features in the Zn 2p spectrum is consistent with the closed-shell d^{10} configuration of Zn^{2+} [65]. The SEM images of the MPor-Py POPs in Fig. S10 reveal the presence of spherical clusters, which likely result from self-assembly driven by strong π-π interactions and the inherent porosity of these samples. Importantly, no significant morphological degradation is observed after metalation, thereby indicating that the overall framework remains intact. Furthermore, the TEM images in Fig. S11 confirm the amorphous nature of the MPor-Py POPs, as evidenced by PXRD shown in Fig. S12 displayed the absence of any long-range order or crystalline lattice fringes.

3.3. *Theoretical calculation of non-metalated and metalated porous organic polymers*

Critical insights into the reactive sites, charge distribution, and electronic behavior of the investigated system are provided by the

molecular electrostatic potential (MESP) maps in Fig. 3. As detailed in the Supporting Information, the polymeric structure was simplified to a representative monomeric repeating unit consisting of one porphyrin moiety and one pyrene moiety for computational efficiency. Thus, while the non-metalated Por-Py POP exhibits distinct, well-defined charge distributions across its conjugated framework, the metal incorporation redistributes the electron density to result in a more balanced and delocalized charge distribution (Fig. 3), which is expected to facilitate efficient charge transport and, hence, an enhanced electrical conductivity. Among the various MPor-Py POPs, the ZnPor-Py POP, featuring a redox-inactive Zn center, shows a more uniform and less strongly bound electrostatic potential within the porphyrin ring. The calculated binding energies of the investigated MPor-Py POPs at the B3LYP/6-31g (d, p) level follow the order: ZnPor-Py POP (−34.16 eV) < CuPor-Py POP (−35.73 eV) < FePor-Py POP (−36.59 eV). This trend is consistent with the experimentally determined metalation efficiencies obtained from ICP-MS analysis, where stronger binding energies correspond to higher degrees of metal incorporation (Tables S2–S4). The relatively weaker Zn-porphyrin coordination arises from the closed-shell configuration of Zn^{2+} ions. Due to the low energy of the Zn d_π orbitals, zinc exerts only a subtle effect on the porphyrin π-π* energy gap. Nevertheless, these low-energy d_π orbitals can effectively interact with the π orbitals of CNTs, thereby enhancing both the d_π-π and π-π interactions between the Zn-porphyrin moieties and the CNTs. Such strengthened interfacial interactions are expected to influence the charge transport and thereby impact the overall TE behavior [43].

To provide insight into the electronic restructuring induced by metal incorporation, the HOMO-LUMO orbitals of non-metalated Por-Py POP and its metalated derivatives (MPor-Py POP, M = Fe^{2+}, Cu^{2+}, and Zn^{2+}) are illustrated in Fig. S13. Thus, in the pristine Por-Py POP, the frontier orbitals are primarily localized on the conjugated aromatic backbone and porphyrin peripheral arms. The LUMO is extensively delocalized, spanning both the porphyrin periphery and adjacent aromatic rings, whereas the HOMO orbitals are primarily localized on the pyrene branches. Upon metalation, the electron-deficient metal centers perturb the electronic distribution, thereby generating more pronounced LUMO features in the CuPor-Py POP and ZnPor-Py POP. Notably, in the FePor-Py POP complex, the Fe-centered orbital interacts strongly with the porphyrin core, which results in LUMO localization predominantly at the metal center and along the porphyrin peripheral arms, with no localization in the adjacent aromatic rings. This LUMO localization is unique to the FePor-Py POP and aligns well with its highest binding energy, thereby indicating the strongest metal–porphyrin coordination among the various complexes. Furthermore, the bandgap evolution among the metalated derivatives follows the order: FePor-Py POP < ZnPor-Py POP < CuPor-Py POP, which can be attributed to variations in the LUMO energy levels and metal–ligand interactions within the complexes.

3.4. Thermoelectric performance of composite films

The above comprehensive structural and morphological characterizations confirmed that the MPor-Py POPs possess amorphous, π-conjugated porous frameworks, which are advantageous for TE applications due to their ability to enhance phonon scattering while offering tunable electronic properties. Moreover, the roles of the metal-ligand binding energies were further elucidated through DFT simulations, which revealed their influence on the interfacial interactions between MPor-Py POPs and CNTs. Based on those structural and theoretical insights, composite thin films containing CNTs in combination with either the pristine Por-Py POP or the various MPor-Py POPs were fabricated to enable a systematic investigation of how the molecular-level interactions translate into macroscopic TE performance. As shown in Fig. S14, solvent selection plays a decisive role in regulating the morphology of the non-metalated Por-Py POP, which in turn governs the quality of the resulting POP-CNT interface. Thus, the dispersion of Por-Py POP in 1,2-dichlorobenzene (DCB) exhibits a uniform spherical morphology, while that in ethanol (EtOH) and *N*-methyl-2-pyrrolidone (NMP) exhibits flake-like aggregation due to stronger self-assembly interactions. Based on these observations, DCB was selected as the processing solvent to ensure a favorable morphology and interfacial compatibility in the resulting MPor-Py POP/CNT composite thin films. The composite thin film fabrication process is detailed in the Experimental section and illustrated in Scheme S1. The influence of composition on the TE performance is elucidated by the electrochemical measurements for the composite films with POP/CNT weight ratios of 1/2, 1/1, and 2/1 in Fig. 4 and Table S5. Thus, all samples display positive Seebeck coefficients [Fig. 4(a)], which are consistent with the p-type doping behavior typically induced by DCB in CNT-based systems [66]. Notably, the Seebeck coefficient increases with the increase in POP content, rising from 34.8 ± 5.2 μV K^{-1} at a 1/1 POP/CNT ratio to 44.4 ± 4.9 μV K^{-1} at 2/1 POP/CNT. This is likely due to enhanced hole transport enabled by the extended π-conjugated backbone of the porphyrin and pyrene units. Importantly, differently metalated samples

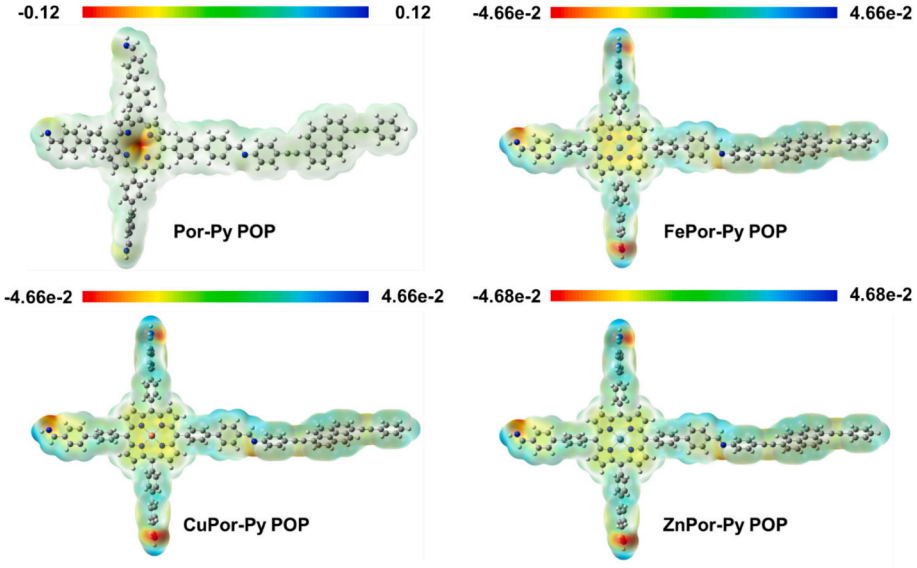

Fig. 3. The MESP maps of pristine Por-Py POP and its metalated derivatives.

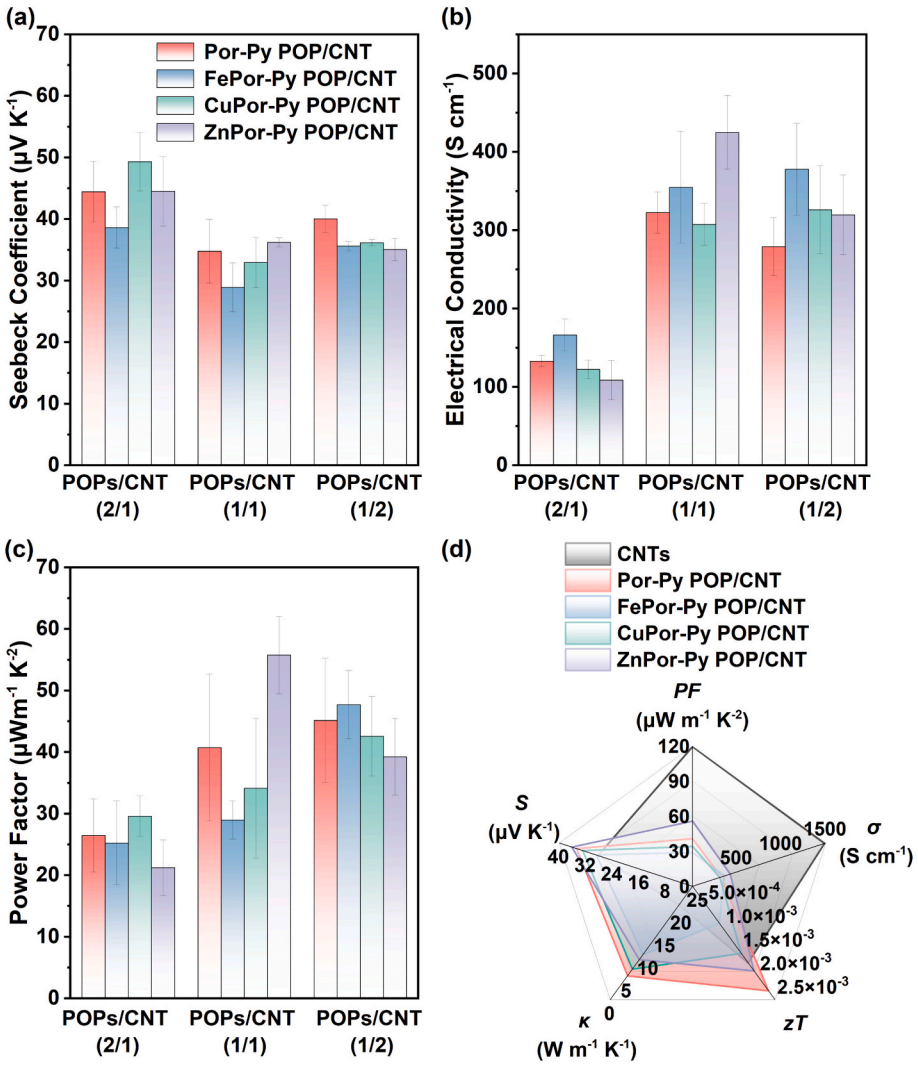

Fig. 4. (a) *S*, (b) *σ*, and (c) *PF* of POP/CNT composite films. (d) Radar plot comparing the overall TE performance parameters of pristine CNTs and POP/CNT composites.

with the same weight ratios display comparable Seebeck coefficients. For example, at a 1/1 weight ratio, the Seebeck coefficient is 34.8 ± 5.2, 28.9 ± 4.0, 33.0 ± 4.1, and 36.2 ± 0.7 μV K^{-1} for the pristine Por-Py POP/CNT, FePor-Py POP/CNT, CuPor-Py POP/CNT, and ZnPor-Py POP/CNT, respectively. This suggests that metal coordination has a limited direct influence on the Seebeck coefficient at a given composition. Meanwhile, at the same weight ratio of 1/1, electrical conductivity values of 322.6 ± 26.4, 354.7 ± 71.3, 307.6 ± 26.5, and 425.0 ± 47.0 S cm^{-1} are measured for the pristine Por-Py POP/CNT, the FePor-Py POP/CNT, the CuPor-Py POP/CNT, and the ZnPor-Py POP/CNT, respectively [Fig. 4(b)]. Here, the higher electrical conductivity values for the Fe- and Zn-containing samples may be attributed to the improved d_{π}-π orbital interactions between the metal ions and CNTs, which lead to facilitated charge transfer. Furthermore, the Hall effect measurements in Table S6 reveal that the inferior electrical conductivity of the Fe- and Cu-based composites mainly arises from reduced carrier concentration rather than severely suppressed mobility. In contrast, the ZnPor-Py POP/CNT composite exhibits a substantially higher carrier concentration, leading to the highest electrical conductivity despite its slightly lower mobility. All composites retain p-type behavior, consistent with the positive Seebeck coefficients and the observed electrical conductivity trends. Additionally, the *PF* of the ZnPor-Py POP/CNT composite is measured as 55.8 ± 6.3 μW m^{-1} K^{-2} [Fig. 4(c)], which represents an ~40% improvement compared to that of its non-metalated Por-Py POP/CNT counterpart (40.7 ± 11.9 μW m^{-1} K^{-2}). This is primarily due to the significantly enhanced electrical conductivity of the metalated form. The electronic configuration of zinc likely plays a key role here: as a closed-shell (d^{10}) metal with low-energy d orbitals, Zn^{2+} does not strongly perturb the porphyrin π-system, thereby preserving its electronic integrity while promoting effective orbital overlap with the π orbitals of the CNTs. By contrast, Fe^{2+} and Cu^{2+} possess partially filled and higher-energy d_{π} orbitals that can introduce stronger orbital mixing and interact with the porphyrin backbone, which potentially disrupts charge delocalization and limits the charge carrier concentration. To further elucidate the structure–activity–performance relationship, we quantitatively correlate metal coordination strength with charge transport parameters obtained from Hall measurements and thermoelectric properties. The results indicate that power factor enhancement arises from coordination-induced interfacial electronic modulation that optimizes the balance between carrier concentration and mobility, rather than from a monotonic increase in metalation degree. To further assess TE performance, the thermal diffusivity (*α*) of each composite thin film with a 1/1 weight ratio was measured by using a thermal wave analyzer, and the corresponding specific heat capacity (*Cp*) was measured via differential scanning calorimetry (DSC). These measurements were then used to calculate the thermal conductivity (*κ*) from Eq. (2):

$$\kappa = \alpha \rho Cp \tag{2}$$

where ρ is the density of the thin film. The results are summarized in Fig. S15 and Table S7.

Thus, the non-metalated Por-Py POP/CNT composite exhibits the lowest thermal conductivity of 5.1 ± 0.3 W m^{-1} K^{-1}, which is attributed to the inherently porous framework of the POP matrix, which effectively enhances phonon scattering and suppresses the thermal conductivity. This thermal suppression contributes to a 34% improvement in zT (2.41 × 10^{-3} ± 0.72 × 10^{-3} at 300 K) compared to the pristine CNTs (1.74 × 10^{-3} ± 0.52 × 10^{-3}). By contrast, while the ZnPor-Py POP/CNT composite achieves the highest *PF*, it exhibits a slightly higher thermal conductivity of 8.8 ± 0.2 W m^{-1} K^{-1}, primarily due to increased electronic thermal conductivity (κ_e) arising from enhanced electrical conductivity, as described by the Wiedemann-Franz law ($\kappa_e = L\sigma T$) [2]. Consequently, the overall TE performance shows a more modest 9.8% increase in zT to 1.89 × 10^{-3} ± 0.22 × 10^{-3}, as shown in Fig. 4(d) and Table S8. When benchmarked against previously reported framework-based thermoelectric materials (Fig. S16 and Table S9), the MPor-Py POP/CNT composites developed in this work exhibit only moderate zT values. This limitation primarily originates from the intrinsically coupled increase in electronic thermal conductivity governed by the Wiedemann-Franz law, as well as differences in thermal conductivity measurement protocols across studies. Nevertheless, the present system demonstrates a clear synergistic regulation of charge transfer and thermal management through a rational framework and interfacial design. These results highlight the effectiveness of integrating π-conjugated networks and metalloporphyrin units into porous organic frameworks to enhance electrical conductivity while suppressing lattice thermal transport, offering a viable strategy for fine-tuning thermoelectric performance.

3.5. *Morphologies, microstructures, and spectral properties of composite films*

The surface morphologies of the optimal TE composite thin films with a mass ratio of 1/1 are characterized by the SEM and AFM images in Figs. 5 and S17–S19. As revealed in Fig. S17, the MPor-Py POPs are uniformly entangled with the CNTs, thereby indicating intimate interfacial contact. Further, the effects of metal-CNT orbital interactions on the dispersion behavior are elucidated by the average CNT bundle sizes for each composite system in Fig. 5. Here, except for pristine CNTs, the ZnPor-Py POP/CNT composite (Fig. 5(e) and (f)) exhibits the smallest bundle size, thereby indicating more effective CNT dispersion. This is attributed to favorable d_π-π orbital interactions between the Zn^{2+} centers (with closed-shell d^{10} configurations and lower energy d_π orbitals) and the π-electron system of the CNTs. By contrast, Fe^{2+} (Fig. 5(c) and

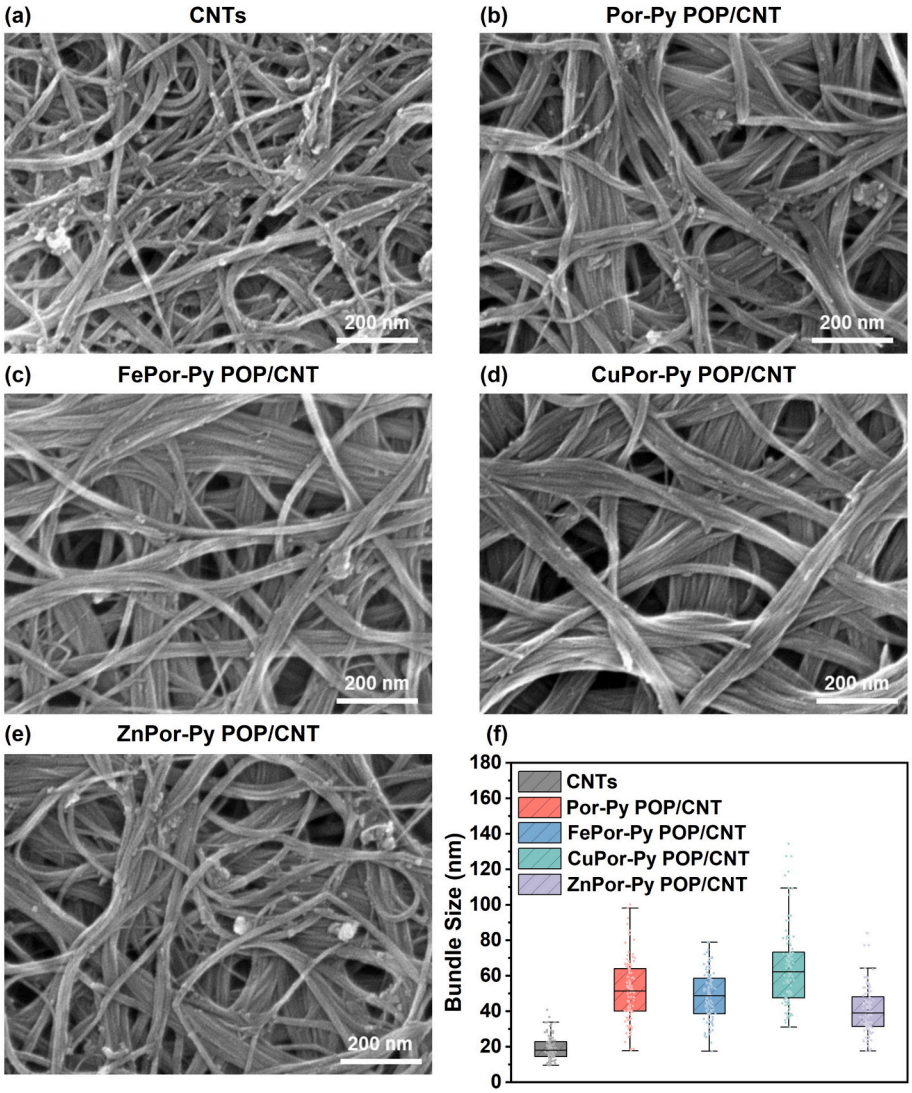

Fig. 5. SEM images of (a) CNTs, (b) Por-Py POP/CNT, (c) FePor-Py POP/CNT, (d) CuPor-Py POP/CNT, (e) ZnPor-Py POP/CNT. All SEM images share the same scale bar (200 nm). (f) Statistical analysis of CNT bundle diameters (100 counts) for each sample.

(f)) and Cu^{2+} (Fig. 5(d) and (f)), which have partially filled, higher-energy d_π orbitals, tend to preferentially coordinate with the porphyrin backbone. This interaction may reduce direct interactions with the CNTs, thus resulting in broader bundle sizes, weaker interfacial contact, and ultimately reduced electrical conductivity. A similar trend is observed in the AFM images (Figs. S18 and S19), where hybridization has resulted in more defined fiber-like morphologies with reduced surface roughness compared to the pristine CNT film, thereby indicating improved CNT dispersion and less aggregation. Notably, the ZnPor-Py POP/CNT composite exhibits the smoothest surface and most uniform topography, with a root-mean-square roughness (R_{rms}) of 9.92 nm (Fig. S18). This is consistent with the SEM observations in Fig. 5(e). This morphological uniformity contributes to more efficient charge transport pathways and explains the superior *PF* of the ZnPor-Py POP/CNT composite. The microstructures of the various thin films are further revealed by the grazing incidence X-ray diffraction (GIXRD) results in Figs. S20 and S21. Here, the MPor-Py samples exhibit broad diffraction halos, which are characteristic of a predominantly amorphous network. Upon incorporation of CNTs, however, the diffraction halos become broader, thereby suggesting that the hybridization disrupts the self-aggregated domains of the polymer while maintaining the disordered microstructure. The absence of sharp diffraction peaks confirms the lack of long-range crystallinity, which is consistent with the amorphous nature of both the MPor-Py POPs and the composite films.

The Raman spectra of the pristine CNTs and various MPor-Py POP/CNT composites are shown in Fig. 6(a), featuring the characteristic radial breathing mode (RBM) at 80–240 cm^{-1}), along with the D, G, and G′ bands at ~1340, 1580, and 2660 cm^{-1}, respectively. The D band originates from disorder-induced vibrations associated with structural defects [67], while the G band corresponds to the intrinsic graphite-related vibrational mode of sp^2-hybridized carbon. The intensity ratio of these two bands (I_D/I_G) provides a qualitative measure of structural defects. Notably, across all composites, the I_D/I_G remains comparable to that of pristine CNTs, thereby indicating that the hybridization process does not introduce significant additional defects or disrupt the graphitic structure of the CNTs. In addition, the interfacial electronic interactions can be probed by examining the spectral shifts in the G band. As shown in Fig. 6(b), the G band of the ZnPor-Py POP/CNT composite undergoes a noticeable blue shift, which is indicative of enhanced p-type doping. This shift implies electron withdrawal from the CNT π-system by the ZnPor-Py POP matrix and correlates well with the elevated electrical conductivity observed for this composite [68]. Such spectral evidence reinforces the notion that Zn^{2+} coordination promotes favorable charge transfer and modulates the electronic structure of the CNTs. Moreover, a closer analysis of the RBM region at 150–240 cm^{-1} (Fig. S22) reveals a marked decrease in RBM intensity for all of the MPor-Py POP/CNT composites compared to the pristine CNTs. This indicates the wrapping of CNTs by the polymer matrix, which suppresses the RBM signal and signifies close interfacial contact [69]. Among the samples, the ZnPor-Py POP/CNT composite exhibits the most pronounced RBM reduction, which further confirms the enhanced interaction between the POP and CNT interface. Furthermore, the work function (W_f) of each composite film, as determined by ultraviolet photoelectron spectroscopy (UPS) and summarized in Fig. S23 and Table S10, is slightly higher than that of the pristine CNTs, thereby confirming the p-type doping effect. In particular, the ZnPor-Py POP/CNT thin film exhibits the highest W_f, in agreement with its strongest doping effect and effective modulation of the CNT electronic properties via Zn^{2+} coordination.

The solid-state UV–vis absorption spectra of the Por-Py POPs, MPor-Py POPs, and their composites are shown in Fig. S24. Here, each metalated sample exhibits a notable decrease in absorption intensity, particularly for the characteristic porphyrin-associated bands, upon the incorporation of CNTs, thereby indicating effective adsorption of the POP framework onto the CNT surfaces. Additionally, the Q bands of the various composites display redshifted and broadened features, which are typically attributed to strong π-π interactions between the porphyrin macrocycles and CNTs [70]. These broadened and shifted absorption features reflect increased electronic delocalization and enhanced orbital overlap, thereby supporting the formation of electronically coupled nanocomposites with intimate interfacial contact. The electronic interactions between MPor-Py POPs and CNTs are further elucidated by the solution-state photoluminescence (PL) spectra in Fig. S25. Here, the pristine MPor-Py POPs each display a primary fluorescence emission centered at ~524 nm, arising from the pyrene units [41], accompanied by two longer-wavelength emissions at 658 and 723 nm, corresponding to the porphyrin moieties [57]. Notably, the ZnPor-Py POP exhibits an extra emission peak at 602 nm, which can be attributed to the formation of a Zn-porphyrin coordination complex [71]. Upon hybridization with CNTs, the PL spectra of the various MPor-Py POP/CNT composites each reveal complete quenching of the pyrene emission, thereby suggesting that the pyrene segments preferentially interact with the CNT surfaces, most likely via π-π stacking. This interaction facilitates non-radiative

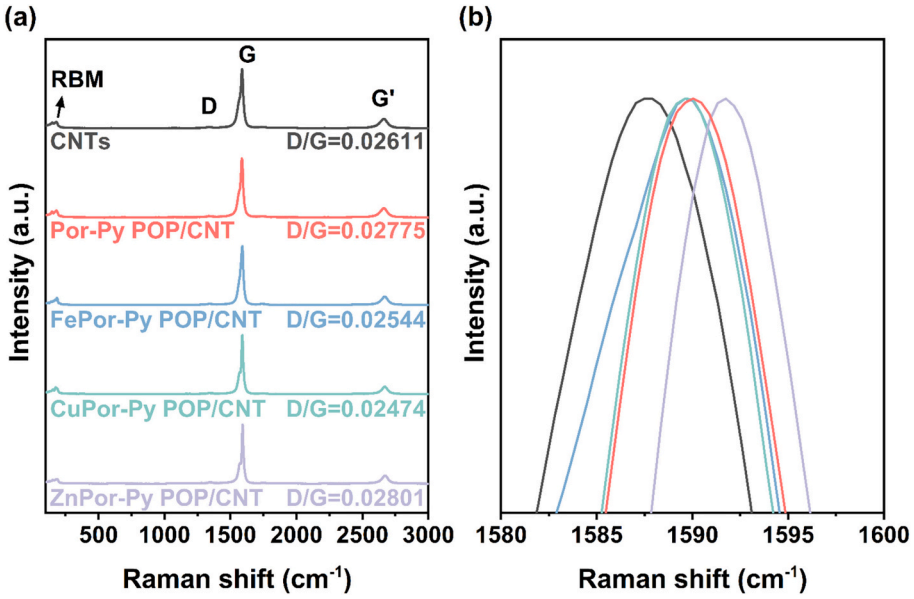

Fig. 6. (a) Full-range Raman spectra and (b) enlarged view of the G-band region of pristine CNTs and POP/CNT composite thin films.

energy or charge transfer from the photoexcited POP backbone to the CNTs, thereby suppressing fluorescence emission. The degree of this interfacial interaction is quantitatively assessed by calculating the photoluminescence quenching efficiency (*PLQE*), as per Eq. (3): [28]

$$\mathrm{PLQE}(\%) = \frac{I_0 - I}{I_0} \times 100 \quad (3)$$

where I_0 corresponds to the strongest fluorescence peak of the pristine MPor-Py POP, and I is that of the corresponding composite. As summarized in Table S11, the ZnPor-Py POP/CNT composite exhibits the highest *PLQE* value of all, at 73.73%, thereby suggesting the strongest interaction and most effective wrapping of POP molecules around the CNTs. These observations are consistent with the above Raman and morphological analyses, thereby reinforcing the critical role of Zn^{2+} in promoting favorable orbital overlap and intimate interfacial contact within the composite architecture.

3.6. Demonstration of wearable thermoelectric generator

To demonstrate the practical viability of the ZnPor-Py POP/CNT composite (which exhibited the highest *PF* among the composites studied), an 8-leg thermoelectric generator (TEG) was fabricated. As shown in Fig. 7(a), the legs were connected in series using copper wires and silver paste. The resulting device was evaluated under various temperature gradients (ΔT), and the measured output voltages (V_m) are summarized in Fig. 7(b). Thus, at ΔT values of 13.2, 17.5, 22.5, 27.6, and 32.5 K, the device generates output voltages of 3.65, 5.04, 6.50, 7.98, and 15.6 mV, respectively. These experimental voltages closely match the theoretical voltages (V_{th}) calculated using Eq. (4):

$$V_{th} = S\,N\Delta T \quad (4)$$

where S is the Seebeck coefficient of the ZnPor-Py POP/CNT composite (36.2 μV K^{-1}), and N is the number of thermoelectric legs ($N = 8$). For instance, at $\Delta T = 13.2$ K, the theoretical voltage is calculated as $V_{th} =$ 3.81 mV (Fig. S26), which aligns well with the measured V_m of 3.65 mV. This linear relationship between V_m and ΔT indicates efficient thermal-to-electrical energy conversion, as supported by the intrinsically low thermal conductivity of the composite material. In addition, the maximum output power (P_{max}) and short-circuit current (I_{sc}) are seen to increase with the increase in ΔT [Fig. 7(b)], reaching 65.8 nW and 27.5 μA, respectively, at a ΔT of ~32.5 K. These values indicate the potential of this composite system for low-power energy harvesting applications. As key requirements for wearable electronics, the mechanical flexibility and durability of the system are evaluated by examining the internal resistance under mechanical deformation. As shown in Fig. 7(c), the TEG maintains a stable internal resistance when subjected to bending ratios ranging from 0% (unbent, 10 cm length) to 90% (1 cm radius of curvature). Moreover, even after 1000 bending cycles at a 70% bending ratio (3 cm), no significant degradation in output voltage or internal resistance is observed [Fig. 7(d)], thus highlighting the excellent mechanical robustness of the composite TEG. Finally, a simulated body-heat test was conducted to demonstrate real-world applicability. As shown in Fig. S27, when the TEG is placed on the human forearm with half of the device being insulated by thermal tape to create a temperature gradient, a V_m of 0.4 mV is generated at a ΔT of ~2.4 K. This result confirms the device's practical feasibility for harvesting body heat, thereby suggesting its potential for integration into self-powered wearable systems.

4. Conclusions

Herein, the fabrication and use of metalated porphyrin-pyrene-based porous organic polymers (MPor-Py POPs) for TE energy harvesting were demonstrated for the first time. When combined with carbon nanotubes (CNTs), the ZnPor-Py POP/CNT composite exhibited the most balanced thermoelectric performance, delivering a power factor (*PF*) of 55.8 ± 6.3 μW m^{-1} K^{-2}, which represented a 40% enhancement compared to its non-metalated counterpart (*PF* = 40.7 ± 11.9 μW m^{-1} K^{-2}). Although the enhanced electrical conductivity of ZnPor-Py POP/CNT composite

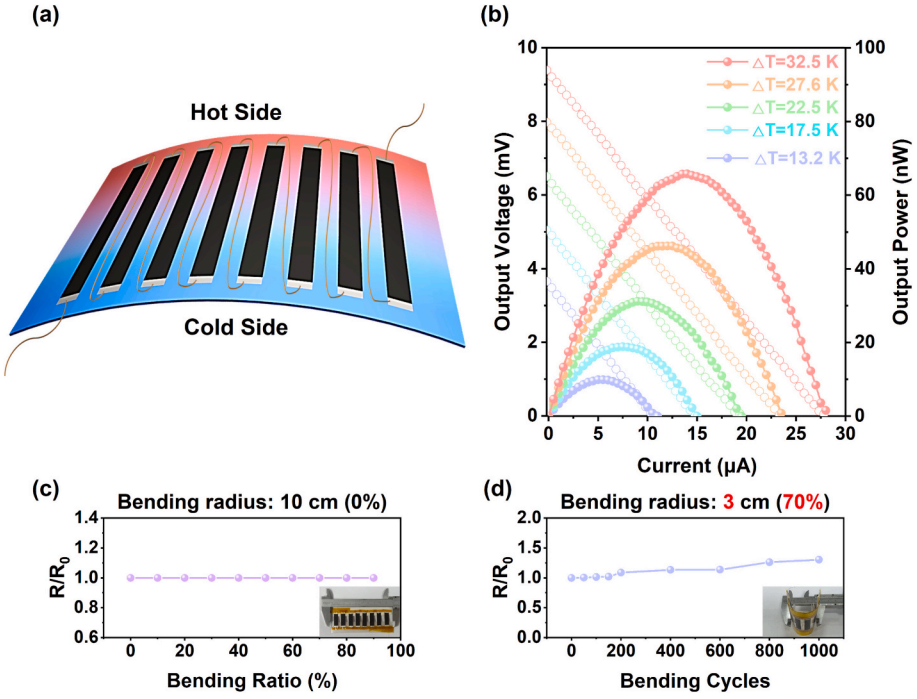

Fig. 7. Demonstration of TEG based on wearable ZnPor-Py POP/CNT composite: (a) schematic illustration of the 8-leg TEG device architecture fabricated from ZnPor-Py POP/CNT composite films. (b) Output characteristics of the TEG under various temperature differences. (c) Internal resistance measurements under different bending ratios, with corresponding photographic images of the TEG in its flat (unbent) state. (d) Internal resistance retention after 1000 mechanical bending cycles at a 70% bending ratio, accompanied by images of the TEG under 70% bending.

inevitably increases the electronic contribution to thermal conductivity (κ_e), the incorporation of a porous and amorphous POP framework is expected to promote phonon scattering and moderate lattice heat transport. As a result, the ZnPor-Py POP/CNT composite exhibits a thermal conductivity (κ) of 8.84 ± 0.2 W m^{-1} K^{-1} and an improved figure of merit (zT) of 1.89 × 10^{-3} ± 0.22 × 10^{-3} at 300 K, corresponding to a 8.6% enhancement over the pristine CNTs (κ = 19.7 ± 5.4 and zT = 1.74 × 10^{-3} ± 0.52 × 10^{-3}). Importantly, the optimized ZnPor-Py POP/CNT composite enabled the fabrication of a flexible 8-leg TEG that maintained a stable electrical output under repeated bending cycles, and demonstrated a robust performance under simulated body-heat conditions, thereby highlighting its potential for wearable applications. These findings not only establish metalated POP/CNT composites as lightweight, flexible, and durable TE materials but also point to future opportunities in molecular design and nanocomposite engineering for further optimization of the zT and integration into next-generation self-powered electronic platforms.

CRediT authorship contribution statement

Tzu-Ling Ma: Writing – review & editing, Writing – original draft, Visualization, Validation, Methodology, Investigation, Formal analysis, Data curation, Conceptualization. **Mohamed Gamal Mohamed:** Methodology, Conceptualization, Formal analysis, Data curation, Writing – original draft, Writing – review & editing, Visualization, Investigation, Supervision. **Hira Karim:** Writing – original draft, Software, Formal analysis. **Shiao-Wei Kuo:** Writing – review & editing, Supervision, Funding acquisition, Conceptualization. **Cheng-Liang Liu:** Writing – review & editing, Supervision, Funding acquisition, Conceptualization.

Declaration of competing interest

The authors declare that they have no known competing financial interests or personal relationships that could have appeared to influence the work reported in this paper.

Acknowledgments

This work was supported by 2030 Cross-Generation Young Scholars Program by the National Science and Technology Council (NSTC) in Taiwan under grant 114-2628-E-002-005, and Academic Research-Career Development Project (Sprout Research Projects) by National Taiwan University (NTU114L7817), and Advanced Research Center for Green Materials Science and Technology from The Featured Area Research Center Program within the framework of the Higher Education Sprout Project by the Ministry of Education (114L9006). The authors acknowledge the mass spectrometry technical research services from the Consortia of Key Technologies, National Taiwan University. Beamtime provided by Beamline TPS25A of the National Synchrotron Radiation Research Center (NSRRC), Taiwan, is gratefully appreciated. We are grateful to Mr. Shing-Jong Huang for assistance in SSNMR, Ms. Su-Jen Ji for the assistance in SEM and Ms. Ya-Yun Yang for the assistance in TEM experiments of the Instrumentation Center at National Taiwan University, supported by the NSTC. We also thank Prof. Chih-I Wu Group of National Science and Technology Council (National Taiwan University) for the assistance in Photoemission spectroscopy (PES) experiments. S. W.K. also acknowledges the financial support from the NSTC under contracts 114-2223-E-110-001 and 113-2221-E-110-012-MY3.

Appendix A. Supplementary data

Supplementary data to this article can be found online at https://doi.org/10.1016/j.cej.2026.174335.

Data availability

Data will be made available on request.

References

[1] J.K. Nøland, M. Hjelmeland, M. Korpås, Will Energy-Hungry AI create a baseload power demand boom? IEEE Access 12 (2024) 110353–110360, https://doi.org/10.1109/ACCESS.2024.3440217.
[2] M. Massetti, F. Jiao, A.J. Ferguson, D. Zhao, K. Wijeratne, A. Würger, J. L. Blackburn, X. Crispin, S. Fabiano, Unconventional thermoelectric materials for energy harvesting and sensing applications, Chem. Rev. 121 (2021) 12465–12547, https://doi.org/10.1021/acs.chemrev.1c00218.
[3] S. Yin, J. Li, Z. Lai, Q.W. Meng, W. Xian, Z. Dai, S. Wang, L. Zhang, Y. Xiong, S. Ma, Q. Sun, Giant gateable thermoelectric conversion by tuning the ion linkage interactions in covalent organic framework membranes, Nat. Commun. 15 (2024) 8137, https://doi.org/10.1038/s41467-024-52487-z.
[4] J. He, T.M. Tritt, Advances in thermoelectric materials research: looking back and moving forward, Science 357 (2017) eaak9997, https://doi.org/10.1126/science.aak9997.
[5] N. Bisht, P. More, P.K. Khanna, R. Abolhassani, Y.K. Mishra, M. Madsen, Progress of hybrid nanocomposite materials for thermoelectric applications, Mater. Adv. 2 (2021) 1927–1956, https://doi.org/10.1039/D0MA01030H.
[6] X.L. Shi, J. Zou, Z.G. Chen, Advanced thermoelectric design: from materials and structures to devices, Chem. Rev. 120 (2020) 7399–7515, https://doi.org/10.1021/acs.chemrev.0c00026.
[7] M. Mukherjee, A. Srivastava, A.K. Singh, Recent advances in designing thermoelectric materials, J. Mater. Chem. C 10 (2022) 12524–12555, https://doi.org/10.1039/D2TC02448A.
[8] M.N. Hasan, H. Wahid, N. Nayan, M.S.M. Ali, Inorganic thermoelectric materials: a review, Int. J. Energy Res. 44 (2020) 6170–6222, https://doi.org/10.1002/er.5313.
[9] S. Zhou, X.L. Shi, L. Li, Q. Liu, B. Hu, W. Chen, C. Zhang, Q. Liu, Z.G. Chen, Advances and outlooks for carbon nanotube-based thermoelectric materials and devices, Adv. Mater. 37 (2025) 2500947, https://doi.org/10.1002/adma.202500947.
[10] J.L. Blackburn, A.J. Ferguson, C. Cho, J.C. Grunlan, Carbon-nanotube-based thermoelectric materials and devices, Adv. Mater. 30 (2018) 1704386, https://doi.org/10.1002/adma.201704386.
[11] Q.X. Hu, W.D. Liu, L. Zhang, W. Sun, H. Gao, X.L. Shi, Y.L. Yang, Q. Liu, Z.G. Chen, SWCNTs/Ag_2Se film with superior bending resistance and enhanced thermoelectric performance via in situ compositing, Chem. Eng. J. 457 (2023) 141024, https://doi.org/10.1016/j.cej.2022.141024.
[12] B. Kumanek, D. Janas, Thermal conductivity of carbon nanotube networks: a review, J. Mater. Sci. 54 (2019) 7397–7427, https://doi.org/10.1007/s10853-019-03368-0.
[13] C. Pramanik, J.R. Gissinger, S. Kumar, H. Heinz, Carbon nanotube dispersion in solvents and polymer solutions: mechanisms, assembly, and preferences, ACS Nano 11 (2017) 12805–12816, https://doi.org/10.1021/acsnano.7b07684.
[14] L. Zhang, Y. Harima, I. Imae, Highly improved thermoelectric performances of PEDOT: PSS/SWCNT composites by solvent treatment, Org. Electron. 51 (2017) 304–307, https://doi.org/10.1016/j.orgel.2017.09.030.
[15] S. Qu, M. Wang, Y. Chen, Q. Yao, L. Chen, Enhanced thermoelectric performance of CNT/P3HT composites with low CNT content, RSC Adv. 8 (2018) 33855, https://doi.org/10.1039/C8RA07297C.
[16] H. Li, S. Liu, P. Li, D. Yuan, X. Zhou, J. Sun, X. Lu, C. He, Interfacial control and carrier tuning of carbon nanotube/polyaniline composites for high thermoelectric performance, Carbon 136 (2018) 292–298, https://doi.org/10.1016/j.carbon.2018.04.083.
[17] Y.T. Lin, C.Y. Lee, C.Y. Wu, J.M. Lin, T.C. Lee, S.H. Tung, C.L. Liu, High thermoelectric performance of spray-coated poly (3, 4-ethylenedioxythiophene): poly (styrenesulfonate) films enabled by two-step post-treatment process, J. Power Sources 556 (2023) 232516, https://doi.org/10.1016/j.jpowsour.2022.232516.
[18] P.S. Lin, S. Inagaki, J.H. Liu, M.C. Chen, T. Higashihara, C.L. Liu, The role of branched alkylthio side chain on dispersion and thermoelectric properties of regioregular polythiophene/carbon nanotubes nanocomposites, Chem. Eng. J. 458 (2023) 141366, https://doi.org/10.1016/j.cej.2023.141366.
[19] T. Fujita, M. Matsuda, P.S. Lin, C.A. Chou, J.M. Lin, C.L. Liu, T. Higashihara, Improved thermoelectric performance of phenylalkyl-substituted polythiophene/single-walled carbon nanotube nanocomposites, J. Colloid Interface Sci. 699 (2025) 138299, https://doi.org/10.1016/j.jcis.2025.138299.
[20] M.H. Lin, S.H. Hong, J.F. Ding, C.L. Liu, Organic porous materials and their nanohybrids for next-generation thermoelectric application, ACS Appl. Mater. Interfaces 16 (2024) 67116–67133, https://doi.org/10.1021/acsami.4c12729.
[21] M.H. Lee, Y.H. Kang, J. Kim, Y.K. Lee, S.Y. Cho, Freely Shapable and 3D porous carbon nanotube foam using rapid solvent evaporation method for flexible thermoelectric power generators, Adv. Energy Mater. 9 (29) (2019) 1900914, https://doi.org/10.1002/aenm.201900914.
[22] U. Ijaz, M. Siyar, C. Park, The power of pores: review on porous thermoelectric materials, RSC Sustain. 2 (2024) 852–870, https://doi.org/10.1039/D3SU00451A.
[23] Y. Fan, Z. Liu, G. Chen, Recent progress in designing thermoelectric metal–organic frameworks, Small 17 (2021) 2100505, https://doi.org/10.1002/smll.202100505.

[24] K. Li, J. Wang, H. Wang, Recent advances of 2D conductive metal–organic frameworks in thermoelectrics, J. Mater. Chem. A 12 (2024) 14245–14267, https://doi.org/10.1039/D4TA01820F.
[25] Y. Xue, Z. Zhang, Y. Zhang, X. Wang, L. Li, H. Wang, G. Chen, Boosting thermoelectric performance by in situ growth of metal organic framework on carbon nanotube and subsequent annealing, Carbon 157 (2020) 324–329, https://doi.org/10.1016/j.carbon.2019.10.049.
[26] C.Y. Lin, J.W. Chang, M.H. Lin, K.C. Wu, S.H. Hong, J.M. Lin, C.W. Kung, C.L. Liu, Carbon nanotube/two-dimensional metal–organic framework composites with enhanced thermoelectric performances for thermoelectric generators, Chem. Eng. J. 521 (2025) 166861, https://doi.org/10.1016/j.cej.2025.166861.
[27] R. Wang, Z. Zhang, J. Qin, Q. Meng, Y. Du, F. Zhang, Nano-/micro-fiber engineering of vinylene-linked polymeric frameworks for flexible free-standing thermoelectric films, Adv. Fiber Mater. 7 (2025) 219–226, https://doi.org/10.1007/s42765-024-00477-7.
[28] M.H. Lin, M.G. Mohamed, C.J. Lin, Y.J. Sheng, S.W. Kuo, C.L. Liu, Achieving high *zT* with carbon nanotube/conjugated microporous polymer thermoelectric Nanohybrids by meticulous molecular geometry design, Adv. Funct. Mater. 34 (2024) 2406165, https://doi.org/10.1002/adfm.202406165.
[29] D. Zhou, K. Zhang, S. Zou, X. Li, H. Ma, Conjugated microporous polymers: their synthesis and potential applications in flexible electrodes, J. Mater. Chem. A 12 (2024) 17021–17053, https://doi.org/10.1039/D4TA02085E.
[30] M.G. Mohamed, A.F.M. El-Mahdy, M.G. Kotp, S.W. Kuo, Advances in porous organic polymers: syntheses, structures, and diverse applications, Mater. Adv. 3 (2022) 707–733, https://doi.org/10.1039/D1MA00771H.
[31] X. Liu, C.F. Liu, S. Xu, T. Cheng, S. Wang, W.Y. Lai, W. Huang, Porous organic polymers for high-performance supercapacitors, Chem. Soc. Rev. 51 (2022) 3181–3225, https://doi.org/10.1039/D2CS00065B.
[32] T. Zhang, V.G. Gregoriou, N. Gasparini, C.L. Chochos, Porous organic polymers in solar cells, Chem. Soc. Rev. 51 (2022) 4465–4483, https://doi.org/10.1039/D2CS00123C.
[33] D.H. Yang, Y. Tao, X. Ding, B.H. Han, Porous organic polymers for electrocatalysis, Chem. Soc. Rev. 51 (2022) 761–791, https://doi.org/10.1039/D1CS00887K.
[34] S. Wang, H. Li, H. Huang, X. Cao, X. Chen, D. Cao, Porous organic polymers as a platform for sensing applications, Chem. Soc. Rev. 51 (2022) 2031–2080, https://doi.org/10.1039/D2CS00059H.
[35] X. Guan, Y. Zhao, H. Pei, M. Zhao, Y. Wang, X. Zhou, M.G. Mohamed, S.W. Kuo, Y. S. Ye, Metalloporphyrin conjugated porous polymer in-situ grown on a Celgard separator as multifunctional polysulfide barrier and catalyst for high-performance Li-S batteries, Chem. Eng. J. 473 (2023) 144733, https://doi.org/10.1016/j.cej.2023.144733.
[36] Y.S. Ye, M.G. Mohamed, W.C. Chen, S.W. Kuo, Integrating the multiple functionalities in metalloporphyrin porous organic polymers enabling strong polysulfide anchoring and rapid electrochemical kinetics in Li–S batteries, J. Mater. Chem. A 11 (2023) 9112–9124, https://doi.org/10.1039/D2TA09232H.
[37] R. Das, P.K. Verma, C.M. Nagaraja, Design of porphyrin-based frameworks for artificial photosynthesis and environmental remediation: recent progress and future prospects, Coord. Chem. Rev. 514 (2024) 215944, https://doi.org/10.1016/j.ccr.2024.215944.
[38] Q.H. Al Galiby, L.A. Algharagholy, H. Sadeghi, V.M.G. Suárez, Highly efficient thermoelectric converters based on metalloporphyrin nanotubes, J. Mater. Chem. A 13 (2025) 9323–9331, https://doi.org/10.1039/D4TA08282F.
[39] J.W. Seng, L. Tong, X.Q. Peng, W.Y. Chang, W. Xie, Y.H. Wang, J.F. Zheng, Y. Shao, J.Z. Chen, S. Jin, X.S. Zhou, Influence of a coordinated metal center on charge transport through a series of porphyrin molecular junctions, J. Phys. Chem. C 126 (2022) 1168–1175, https://doi.org/10.1021/acs.jpcc.1c08667.
[40] A.O. Mousa, S.U. Sharma, S.V. Chaganti, T.H. Mansoure, P.N. Singh, M. Ejaz, C. H. Chuang, J.T. Lee, S.W. Kuo, M.G. Mohamed, Designing strategically functionalized conjugated microporous polymers with pyrene and perylenetetracarboxylic dianhydride moieties with single-walled carbon nanotubes to enhance supercapacitive energy storage efficiency, J. Power Sources 608 (2024) 234624, https://doi.org/10.1016/j.jpowsour.2024.234624.
[41] M.G. Mohamed, A. Basit, C.Y. Shih, S.U. Sharma, T. Mondal, S.W. Kuo, Pyrene-linked covalent organic polymer/single-walled carbon nanotubes hybrids as high-performance electrodes for Supercapacitive energy storage, ACS Appl. Energy Mater. 8 (2025) 3764–3778, https://doi.org/10.1021/acsaem.5c00052.
[42] M.G. Mohamed, B. Halder, P.N. Singh, A.A.K. Mohammed, P. Elumalai, S.W. Kuo, Molecular engineering and synergistic redox-active hexaazatrinaphthalene and pyrene-based conjugated microporous polymers for superior faradaic supercapacitor energy storage, Chem. Eng. J. 520 (2025) 165892, https://doi.org/10.1016/j.cej.2025.165892.
[43] Y. Zhou, Y. Liu, X. Zhou, Y. Gao, C. Gao, L. Wang, High performance p-type organic thermoelectric materials based on metalloporphyrin/single-walled carbon nanotube composite films, J. Power Sources 423 (2019) 152–158, https://doi.org/10.1016/j.jpowsour.2019.03.028.
[44] T. Mondal, M.G. Mohamed, A.A.K. Mohamed, S.W. Kuo, Construction of metal-coordinated Bipyridine-based conjugated microporous polymers as robust Electrocatalysts for hydrogen evolution, ACS Appl. Energy Mater. 8 (2025) 7703–7713, https://doi.org/10.1021/acsaem.5c00992.
[45] M.G. Mohamed, Y.C. Kao, B.X. Su, H. Karim, S.W. Kuo, Strategic molecular engineering of ultrastable porous organic polymer engineered with tetraethynylpyrene-functionalized benzoxazine for superior CO_2 capture via solid-state chemical conversion, Sep. Purif. Technol. 387 (2026) 136692, https://doi.org/10.1016/j.seppur.2025.136692.
[46] M.G. Mohamed, C.C. Chen, S.W. Kuo, Nitrogen and sulfur co-doped microporous carbon through benzo[c]-1,2,5-thiadiazole-functionalized benzoxazine-linkage porous organic polymer in CO_2 capture and energy storage, React. Funct. Polym. 214 (2025) 106286, https://doi.org/10.1016/j.reactfunctpolym.2025.106286.
[47] M. Ejaz, M.G. Mohamed, S.W. Kuo, Benzoxazine-linked polyhedral oligomeric silsesquioxane: 3D porous organic-inorganic polymer for improved CO_2 capture and supercapacitor performance, J. Taiwan Inst. Chem. Eng. (2025) 106098, https://doi.org/10.1016/j.jtice.2025.106098.
[48] W.T. Du, S.Y. Chen, S.W. Kuo, Mesoporous phenolic/carbon materials templated by CO_2-based PEO-*b*-PCHC diblock copolymers through mediated competitive intermolecular hydrogen bonding interactions for CO_2 capture, J. CO_2 Util. 80 (2024) 102702, https://doi.org/10.1016/j.jcou.2024.102702.
[49] X. Tang, Z. Jiang, Z. Li, Z. Gao, Y. Bai, S. Zhao, J. Feng, The effect of the variation in material composition on the heterogeneous pore structure of high-maturity shale of the Silurian Longmaxi formation in the southeastern Sichuan Basin, China, J. Nat. Gas Sci. Eng. 23 (2015) 464–473, https://doi.org/10.1016/j.jngse.2015.02.031.
[50] M.G. Mohamed, S.U. Sharma, P.T. Wang, M. Ibrahim, M.H. Lin, C.L. Liu, M. Ejaz, H.J. Yen, S.W. Kuo, Construction of fully π-conjugated, diyne-linked conjugated microporous polymers based on tetraphenylethene and dibenzo[g,p]chrysene units for energy storage, Polym. Chem. 15 (2024) 2827–2839, https://doi.org/10.1039/D4PY00421C.
[51] K.I. Aly, M.M. Sayed, M.G. Mohamed, S.W. Kuo, O. Younis, A facile synthetic route and dual function of network luminescent porous polyester and copolyester containing porphyrin moiety for metal ions sensor and dyes adsorption, Microporous Mesoporous Mater. 298 (2020) 110063, https://doi.org/10.1016/j.micromeso.2020.110063.
[52] G. Zhang, A.F.M. El Mahdy, L.R. Ahmed, B.M. Matsagar, S. Al Saeedi, S.W. Kuo, K. C.W. Wu, Metal complexes of the porphyrin-functionalized Polybenzoxazine, Polymers 14 (2022) 449, https://doi.org/10.3390/polym14030449.
[53] Y. Zhao, L.J. Gao, W.C. Chen, X. Xu, W.Y. Peng, X.Y. Xiao, H.Y. Liu, L.P. Si, The S-doped cobalt porphyrin-based molecular catalysts with large conjugated meso-substituents for enhanced electrocatalytic oxygen reduction and evolution reaction, J. Electrochem. Soc. 168 (2021) 116502, https://doi.org/10.1149/1945-7111/ ac3273.
[54] M. Kubovics, O. Careta, O. Vallcorba, G.R. Islas, L. Rodríguez, J.A. Ayllón, C. Domingo, C. Nogués, A.M.L. Periago, Supercritical CO_2 synthesis of porous Metalloporphyrin frameworks: application in photodynamic therapy, Chem. Mater. 35 (2023) 1080–1093, https://doi.org/10.1021/acs.chemmater.2c03018.
[55] H. Hu, L. Zeng, Z. Li, T. Zhu, C. Wang, Incorporating porphyrin-Pt in light-harvesting metal-organic frameworks for enhanced visible light-driven hydrogen production, Chin. J. Catal. 42 (2021) 1345–1351, https://doi.org/10.1016/S1872-2067(20)63738-X.
[56] W. Zhen, D.W. Kang, Y. Fan, Z. Wang, T. Germanas, G.T. Nash, Q. Shen, R. Leech, J. Li, G.S. Engel, R.R. Weichselbaum, W. Lin, Simultaneous protonation and metalation of a porphyrin covalent organic framework enhance photodynamic therapy, J. Am. Chem. Soc. 146 (2024) 16609–16618, https://doi.org/10.1021/jacs.4c03519.
[57] N.M.M. Moura, S. Valentini, V. Cheptene, A. Pucci, M.G.P.M.S. Neves, J.L. Capelo, C. Lodeiro, E. Oliveira, Multifunctional porphyrin-based dyes for cations detection in solution and thermoresponsive low-cost materials, Dyes Pigments 185 (2021) 108897, https://doi.org/10.1016/j.dyepig.2020.108897.
[58] J. Wei, D. Wang, J. Li, J. Zhang, N. Wang, J. Li, A benzimidazole-linked porphyrin covalent organic polymers as efficient heterogeneous catalyst/photocatalyst, Appl. Organomet. Chem. 36 (2022) e6820, https://doi.org/10.1002/aoc.6820.
[59] O.J. Achadu, M. Managa, T. Nyokong, Fluorescence behaviour of supramolecular hybrids containing graphene quantum dots and pyrene-derivatized phthalocyanines and porphyrins, J. Photochem. Photobiol. A Chem. 333 (2017) 174–185, https://doi.org/10.1016/j.jphotochem.2016.10.029.
[60] M.A. Bouicha, C. Mabrouk, B. Gassoumi, H. Barhoumi, F. Molton, F. Loiseau, T. Roisnel, A.S. Medina, J.M.C. Bravo, E.A. Lopez Maldonado, H. Nasri, New zinc (ii) metalloporphyrin: molecular structure, spectroscopic characterization, electrochemical sensing of dopamine, and catalytic dye degradation, RSC Adv. 15 (2025) 9810–9827, https://doi.org/10.1039/D5RA00762C.
[61] I. Osadchuk, R. Aav, V. Borovkov, E. Clot, Chirogenesis in zinc porphyrins: theoretical evaluation of electronic transitions, controlling structural factors and axial ligation, ChemPhysChem 22 (2021) 1817–1833, https://doi.org/10.1002/cphc.202100345.
[62] J. Yu, Q.M. Hasi, Y. Guo, L. Song, M. Yin, L. Ma, Z. Han, C. Xiao, Y. Zhang, L. Chen, Porphyrin-based conjugated microporous polymer loaded with nanoscale Zerovalent Iron for the degradation of organic pollutants under visible light, Langmuir 40 (2024) 4739–4750, https://doi.org/10.1021/acs.langmuir.3c03507.
[63] S. Hu, Y. Jia, Function of tetra (4-Aminophenyl) porphyrin in altering the electronic performances of reduced graphene oxide-based field effect transistor, Molecules 24 (2019) 3960, https://doi.org/10.3390/molecules24213960.
[64] A.M. El-Mahalawy, A.M. Nawar, A.R. Wassel, Efficacy assessment of metalloporphyrins as functional materials for photodetection applications: role of central tetrapyrrole metal ions, J. Mater. Sci. 57 (2022) 15413–15439, https://doi.org/10.1007/s10853-022-07574-1.
[65] S. Chen, M. Liao, X. Li, R. Li, J. Zhang, Y. Zhang, T. Peng, Metal center regulation of the porphyrin unit in covalent organic polymers for boosting the photocatalytic CO_2 reduction activity, Catal. Sci. Technol. 12 (2022) 6527–6539, https://doi.org/10.1039/D2CY01473D.
[66] Y. Wang, Q. Li, J. Wang, Z. Li, K. Li, X. Dai, J. Pan, H. Wang, Understanding the solvent effects on polarity switching and thermoelectric properties changing of solution-processable n-type single-walled carbon nanotube films, Nano Energy 93 (2022) 106804, https://doi.org/10.1016/j.nanoen.2021.106804.

[67] M.S. Dresselhaus, G. Dresselhaus, A. Jorio, A.G.S. Filho, R. Saito, Raman spectroscopy on isolated single wall carbon nanotubes, Carbon 40 (2002) 2043–2061, https://doi.org/10.1016/S0008-6223(02)00066-0.
[68] Q. Guo, X. Wang, P. Zhao, Z. Zhang, L. Geng, Y. Liu, Y. Teng, Y. Zhong, L. Kang, Performance enhancement of carbon nanotube network transistors via SbI_3 inner-doping in selected regions, Adv. Mater. 37 (2025) 2415442, https://doi.org/10.1002/adma.202415442.
[69] W.C. Shih, M. Matsuda, K. Konno, P.S. Lin, T. Higashihara, C.L. Liu, Tailored thermoelectric performance of poly(phenylene butadiynylene)s/carbon nanotubes nanocomposites towards wearable thermoelectric generator application, Compos. Part B Eng. 286 (2024) 111779, https://doi.org/10.1016/j.compositesb.2024.111779.
[70] H.Z. Zhao, Y.Y. Chang, C. Liu, Electrodes modified with iron porphyrin and carbon nanotubes: application to CO_2 reduction and mechanism of synergistic electrocatalysis, J. Solid State Electrochem. 17 (2013) 1657–1664, https://doi.org/10.1007/s10008-013-2027-1.
[71] B.B. Beyene, A.W. Yibeltal, M.T. Ayana, Colorimetric and fluorescent on-off detection of Cu^{2+}, Sn^{2+} and Zn^{2+} by a water-soluble porphyrin: electronic absorption and emission study, Results Chem. 2 (2020) 100058, https://doi.org/10.1016/j.rechem.2020.100058.